Available online at www.sciencedirect.com
SCIENCE DIRECT
Nuclear Instruments and Methods in Physics Research A 560 (2006) 395–404
NUCLEAR INSTRUMENTS & METHODS IN PHYSICS RESEARCH Section A
www.elsevier.com/locate/nima

Response of the GLAST LAT calorimeter to relativistic heavy ions

B. Lott[a,*], F. Piron[b], B. Blank[a], G. Bogaert[c], J. Bregeon[a], G. Canchel[a], A. Chekhtman[d], P. d'Avezac[c], D. Dumora[a], J. Giovinazzo[a], J.E. Grove[d], M. Hellström[e], A. Jacholkowska[b], W.N. Johnson[d], E. Nuss[b], Th. Reposeur[a], D.A. Smith[a], K. Sümmerer[e], for the GLAST collaboration

[a]*Centre d'Etudes Nucléaires de Bordeaux-Gradignan, CNRS/IN2P3-Université Bordeaux 1, Domaine du Haut Vigneau, BP 120, F-33175 Gradignan Cedex, France*
[b]*Laboratoire de Physique Théorique et d'Astroparticules, Université de Montpellier II, Place Eugene Bataillon, F - 34095 Montpellier Cedex 5, France*
[c]*Laboratoire Leprince-Ringuet, Ecole Polytechnique, Route de Saclay, F-91128 Palaiseau Cedex, France*
[d]*Naval Research Laboratory, Code 7651, 4555 Overlook Avenue, Washington, DC 20375-6817, USA*
[e]*Gesellschaft für Schwerionenforschung, Planckstrasse 1, D-64291 Darmstadt, Germany*

Received 17 December 2005; accepted 17 December 2005
Available online 17 January 2006

Abstract

The CsI calorimeter of the Gamma-Ray Large-Area Space Telescope (GLAST) will be calibrated in flight with cosmic-ray heavy ions. In order to determine the response of the calorimeter to relativistic heavy ions lighter than Fe, an experiment was carried out at the GSI heavy ion facility using the Fragment Separator (FRS). The measured response exhibits an unexpected feature for light ions, opposite to that observed at low incident energy: for a given deposited energy, the observed signal is greater for these ions than for protons (or more generally $Z = 1$ minimum ionizing particles). Pulse shapes are found to be almost identical for carbon ions and $Z = 1$ particles, with a significant slow scintillation component, which constitutes another departure from the low-energy behavior. Data on the energy resolution for the individual CsI crystals and on the loss of ions due to nuclear reactions in the calorimeter are also presented.
© 2006 Elsevier B.V. All rights reserved.

PACS: 29.40.Mc; 95.55.Ka

Keywords: Scintillation; Relativistic heavy ions; CsI; Calorimeter

1. Introduction

The Gamma-Ray Large-Area Space Telescope (GLAST) [1] is the next generation high-energy gamma-ray satellite, to be launched by NASA in 2007. GLAST's main instrument, the large area telescope (LAT) [2] will cover the energy range between 20 MeV and 300 GeV. The LAT will comprise three subsystems: a tracker made of 18 layers of crossed silicon strips interlaced with W converter foils, wherein the incident gamma ray converts into a e^+e^- pair, a CsI calorimeter (8.5 radiation lengths in thickness, made of 1536 crystals) sampling the electromagnetic-shower energy, and an anticoincidence shield for vetoing charged cosmic rays. The LAT will be composed of 16 elements called towers, each made of a tracker and a calorimeter module.

In orbit, the energy calibration and the response monitoring of the calorimeter will exploit the energy deposits of cosmic-ray heavy ions (essentially C, N, O, Si and Fe). Fig. 1 displays a typical energy spectrum of carbon ions at GLAST's flight altitude (565 km), as calculated with the code CREME [3]. This spectrum is depleted at low energy due to the geomagnetic cutoff and peaks around 4 GeV/nucleon. Within the calorimeter, most ions will induce nuclear reactions with Cs or I nuclei. The others (less than 30% for Fe) will only suffer ionization energy loss. As the ion energies are close to

*Corresponding author.
E-mail address: lott@cenbg.in2p3.fr (B. Lott).

0168-9002/$ - see front matter © 2006 Elsevier B.V. All rights reserved.
doi:10.1016/j.nima.2005.12.211

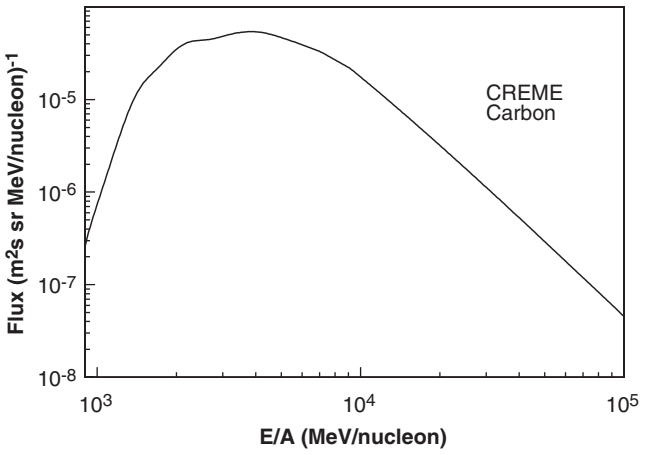

Fig. 1. Kinetic-energy distribution of cosmic-ray carbon ions at GLAST flight altitude as calculated with CREME.

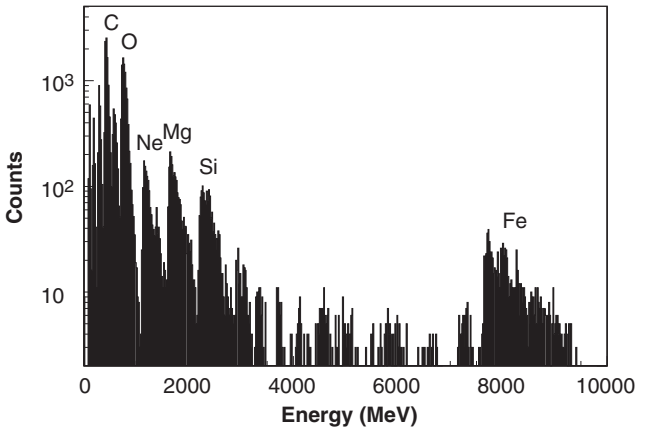

Fig. 2. Expected distribution of ionization energy deposited by the cosmic-ray ions in one CsI crystal, corrected for geometrical effects due to slanted trajectories. The main peaks are labeled according to the elements they correspond to.

the minimum-ionization energy (about 2 GeV/nucleon) and correspond to the "logarithmic rise" part of the energy-loss curve, the distributions of ionization energy deposited within the 1.99 cm-thick CsI crystals, will exhibit well-defined peaks, each corresponding to a different element (Fig. 2), after correction for geometrical effects. The energy calibration can be established by comparing the actual peak positions with those predicted by Monte-Carlo simulations, such as those used to produce the spectrum in Fig. 2. It must be stressed that although the Fe peak is broad, its low-energy edge is well defined. This edge is located around 7.7 GeV: for orientation, the average energy deposited at the maximum of the longitudinal energy deposition profile for an on-axis 300 GeV gamma-ray is about 25 GeV. This method thus provides an adequate coverage over most of the useful energy range.

This calibration procedure necessitates the prior knowledge of the response of the CsI crystals to the relativistic ions of interest. It has been long known that both organic and inorganic scintillators exhibit non-linear responses [4] to highly ionizing particles, like ions: the high ionization density created around the ion path leads to quenching interactions between the excited molecules, in which part of the energy goes into non-radiative decay channels. The "activator-depletion hypothesis" [5] provides a simple explanation for the quenching effect: as the electron–hole pair density increases, the number of unoccupied Tl sites shrinks and the remnant electron–hole pair density cannot contribute to scintillation for lack of available Tl sites. However, numerous studies have proved that reality is more complex and that other processes are involved. These include non-radiative excitations with a probability scaling quadratically with the pair density [6] or the destruction of electron–hole pairs at excited activator sites [6], or merely direct recombination. A precise determination of the amount of produced light as a function of the deposited energy, $L(E)$, must be performed from accelerator data. Although several studies have been devoted to determining this function at low incident energy [7], there has been no work dedicated to CsI beyond 100 MeV/nucleon to the best of our knowledge, and very little to other inorganic scintillators [8,9]. The scarcity of data stems from the fact that scintillation detectors are inappropriate for measuring the total kinetic energy of relativistic ions in standard nuclear physics experiments: the ion range in the detector becoming comparable to the interaction length as the ion energy increases, the probability for an ion undergoing a nuclear reaction within the detector becomes exceedingly high.

We define the quenching factor as the ratio $\alpha S_{\text{part}}/E_{\text{dep}}$ where S_{part} is the measured signal for a given particle and is proportional to the collected light, E_{dep} is the calculated deposited energy via ionization and α is a constant adjusted so that the quenching factor is 1 for protons, and more generally for $Z = 1$ minimum ionizing particles (MIPs). At low incident energy the quenching factor is observed to be lower than 1. From the trend of low-energy data, it can be expected that this factor increases (and thus that the quenching effect decreases) with the ion kinetic energy, as the result of two concurring effects [5]: the decrease of the ionization density as the deposited energy is lower and the increasing fraction of energy carried off by δ electrons. As δ electrons have a range greater than the radius of the primary column (about 400 nm), they escape the column and produce light with high efficiency in the region of low ionization density.

This paper presents results of an experiment carried out at the Gesellschaft für Schwerionenforschung (GSI, Darmstadt), aiming at determining the quenching factors for relativistic ions lighter than Fe. It made use of the Fragment Separator (FRS), affording a great flexibility in producing and selecting different ion species. The paper is organized as follows: the detector characteristics are presented in Section 2, the data analysis is described in Section 3. The differences observed for ions and protons are discussed in Section 4, in which complementary data concerning the pulse shapes are also presented. Sections 5

and 6 present additional results relevant to the in-flight calibration, on the detector energy resolution and the loss of ions due to nuclear reactions, respectively. Conclusions are given in Section 7.

2. Detector characteristics

A prototype calorimeter module known as the Engineering Model (EM) was used in the experiment. It comprises eight crossed layers of 12 CsI crystals, 32.6 cm × 2.67 cm × 1.99 cm in dimensions, sitting in individual cells made of carbon fibers. In the experiment, the crystal main axis was horizontal for odd-labeled layers and vertical for even-labeled ones. Each crystal is read out at each end by two photodiodes, a large one ($1.5\,cm^2$) and a small one ($0.25\,cm^2$). Each photodiode is associated with two electronic chains with different gains, leading to a total of four energy ranges with approximate full-scale values: 200 MeV, 1.6, 12, 100 GeV (referred to as LEX8, LEX1, HEX8, HEX1 in the following, respectively). The crystal light taper, corresponding to the light attenuation along its main axis, allows the hit position along the crystal axis to be inferred from the relative amount of light measured at each end. The EM was fitted with a prototype of the flight electronics, which was very similar to the final one. The analog part consisted of an ASIC (“Application Specific Integrated Circuit”) comprising a charge preamplifier, a shaping amplifier (shaping time: 3.5 μs) and a 12-bit ADC. The latter sampled the amplitude of the analog signal through a Track & Hold stage at a fixed delay time after the trigger signal. This electronics suffered significant integral non-linearity inherent in low-consumption ASICs, which was corrected for using charge-injection measurements.

Another detector, referred to as the Minical, equipped with high-performance, discrete electronics was used alternatively for comparison. It consisted of eight layers of three crystals each, of the same type as for the EM. The electronic chain comprised similar elements as those included in the EM ASICs. The shaping times of the amplifiers were comparable for the two chains. A notable difference was the ADC, as the Minical used a standard, 12-bit peak-sensing ADC (CAEN V785). The Minical was mounted on a moving arm and could taken in and out of the beam in front of the EM. The two detectors had independent VME acquisition systems.

Both detectors were placed close to the FRS final focal plane. Most of the experiment was performed with a primary Ni beam at 1.7 or 1 GeV/nucleon, producing secondary ions (“cocktail beam”) in the Be primary target located at the FRS entrance. Four FRS dipole magnets selected the traversing ions according to their magnetic rigidities and the associated detection system provided for a very precise identification and energy measurement of the ions on an event-by-event basis. The detection system was composed of multiwire proportional counters (MWPC) supplying the ion positions, plastic scintillation detectors enabling time-of-flight measurements, and a segmented ionization chamber, MUSIC, yielding an energy-loss measurement. The EM and Minical were positioned behind the last plastic detector, which provided the trigger signal for the three acquisition systems. The latter operated synchronously (only one of either the EM or the Minical operating at a time), and shared a common veto signal to account for the difference in dead time. The data streams were merged offline. Proper synchronization could be verified using timestamps that were recorded for each event in the different streams.

For cocktail beams, the FRS was tuned on $A/Z = 2$ ions, and the counting rate at the exit was limited to less than 200 Hz. Other runs were carried out with a primary ^{12}C beam, the FRS being tuned so as to provide beams of protons or α particles. For these runs with light particles, the last plastic scintillator was replaced by a 2 cm-thick detector to keep the trigger efficiency high.

3. Description of the analysis

3.1. MUSIC calibration

The incident ions were selected by using the information from the FRS ionization chamber MUSIC (Fig. 3). The signal amplitudes scale with the chamber gas pressure, which is equal to the atmospheric pressure. As a consequence, the MUSIC calibration varied as a function of time. This variation was corrected for over the 10 night duration of the experiment.

3.2. EM energy calibration

The non-linearity correction and pedestal subtraction for all four ranges per crystal were performed using coefficients determined from charge-injection measurements. The absolute energy calibration for the lowest range (LEX8) was established by adjusting the measured deposited-energy distributions obtained for 1.7 GeV protons to the corresponding distributions predicted by GEANT4 [10] (Fig. 4). The latter distributions had to be smeared with a

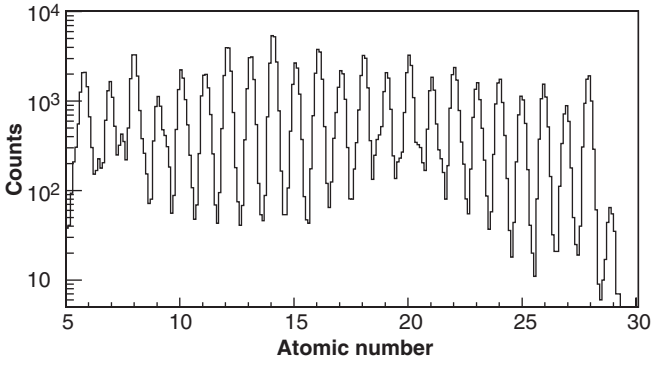

Fig. 3. Atomic number distribution of ions as measured by the FRS ionization-chamber MUSIC for the cocktail-beam runs.

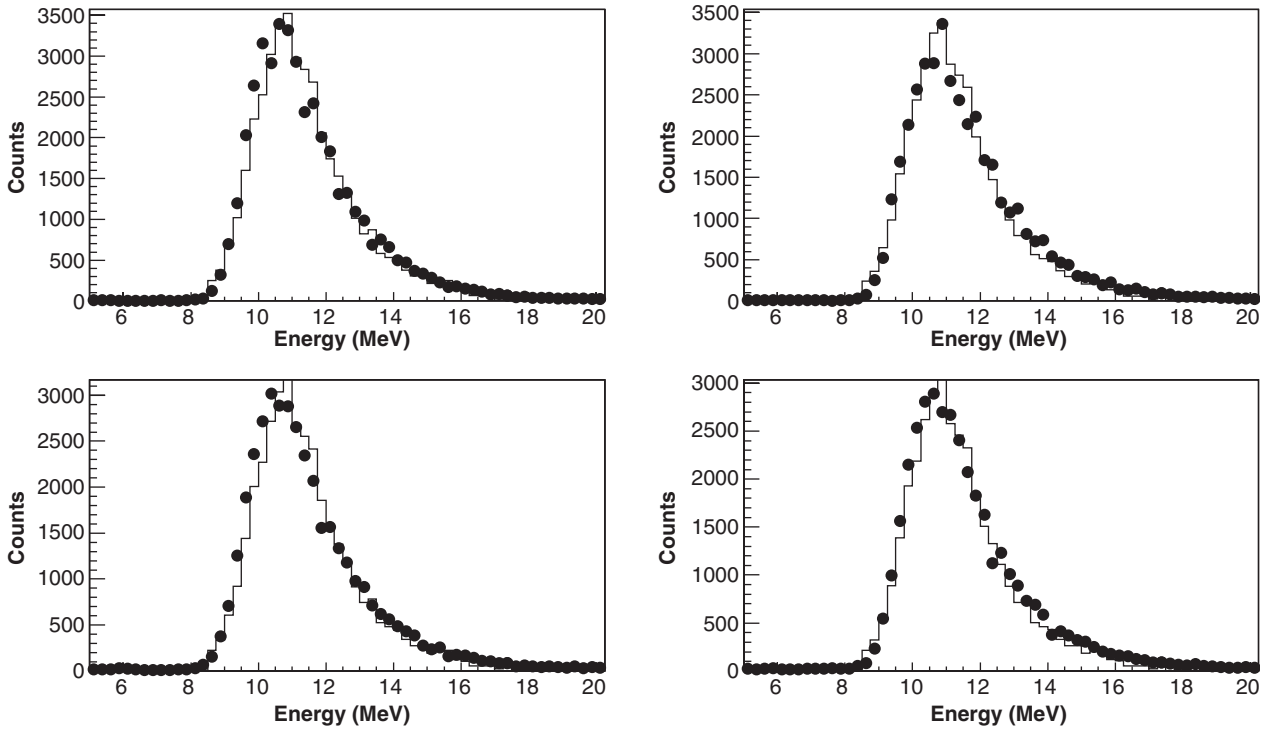

Fig. 4. Calibrated deposited-energy distributions for 1.7 GeV protons (symbols) compared to the corresponding GEANT4 predictions smeared by 0.6 MeV (histograms), for the first four EM layers.

Gaussian distribution of width 0.6 MeV to better reproduce the experimental data (this effect will be further discussed below). Two different calibration procedures were followed: the adjustment between the two distributions was done directly in the first case, while in the second, the two distributions were separately fitted with Landau distributions, and the relative conversion factors were derived from the fit results. The calibration coefficients found in the two procedures are consistent within 0.2% on the average, with a maximum difference of 2.8%.

Cross-calibration between different energy ranges for the same crystal was performed by comparing the data measured in the overlapping regions (about 600 ADC channels—out of 4095—for the upper range) of adjacent ranges. Multiplying the LEX8 calibration coefficients by the thus obtained relative factors provided successively the calibration coefficients for the three upper ranges LEX1, HEX8 and HEX1.

3.3. Minical energy calibration

A similar procedure was followed for the Minical. The proton runs were performed with high-gain amplifiers. The relative electronic gains with respect to the low-gain amplifiers used for the rest of the experiment were established by injecting a similar charge in the preamplifiers and comparing the output amplitudes. The absolute energy calibration derived from the proton data was checked with gamma-rays from a ^{22}Na source. Very good agreement (2%) between the calibration coefficients obtained by the two methods was observed. The calibration was also compared to that established at CERN with 20 GeV muons for the same crystals. Again, the agreement was found to be excellent.

3.4. Quenching determination

The quenching factors, i.e. the ratio between measured and theoretical deposited energy, were obtained for the various incident ions through the following steps.

- The incident ions were selected by using the information from the FRS ionization chamber MUSIC. The resulting deposited-energy distributions measured in the first and last layers are displayed in Fig. 5 for $Z = 8$ (O), $Z = 14$ (Si) and $Z = 20$ (Ca) ions. No geometrical correction had to be applied as the particles traversed the crystal perpendicular to the layer plane. The distributions exhibit a well-defined ionization energy peak and secondary peaks at lower energy corresponding to charge-changing events in which the primary ions lost $1, 2, 3, \ldots$, protons on top of a continuum due to more inelastic nuclear reactions (with deposited energy sometimes exceeding the ionization-peak energy), growing for deeper layers. Most nuclear-reaction events could be eliminated by imposing a selection of the crystal hit multiplicity. It was checked that the peak location remained insensitive to this selection.

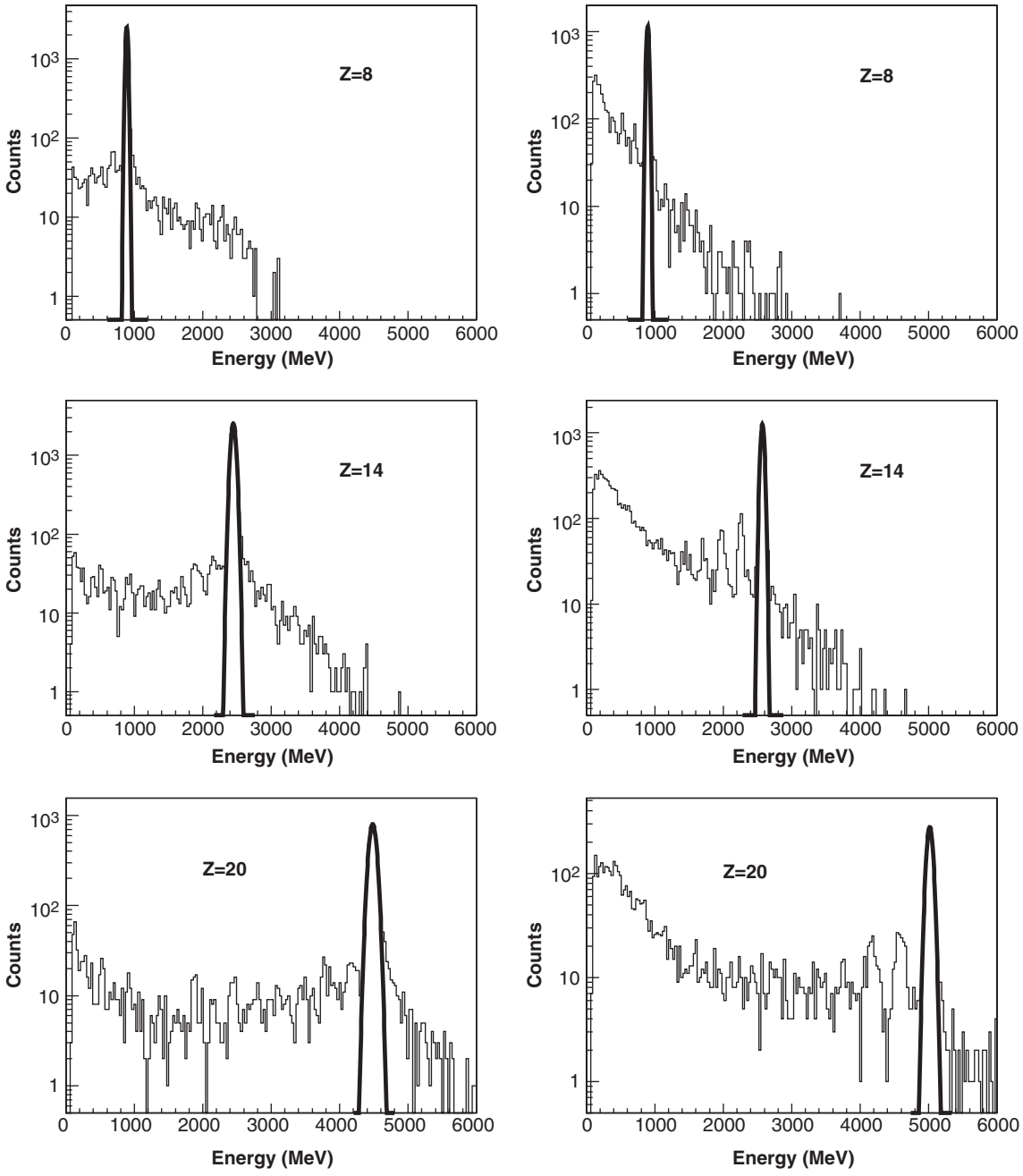

Fig. 5. Deposited-energy distributions measured in the first (left) and last (right) EM layers for 1.7 GeV/nucleon O, Si, Ca ions, from top to bottom, respectively. The secondary peaks at lower energy correspond to charge-changing events in which the primary ions lost 1, 2, 3, ..., protons. The solid curves correspond to the Gaussian fits of the ionization peaks.

- The ionization energy peaks in the ion-selected histograms were fitted with Gaussian functions (solid curves in Fig. 5). The fit was performed independently for each end of the crystal. For the horizontal layers, the ratio of the two means varies significantly with the ion Z, manifesting the lateral dispersion of the ions along the focal plane caused by the spectrometer and stemming from the light attenuation within the crystal ("light tapering"). This dependence is illustrated in Fig. 6 for the first layer. The average of the two energies was considered in the rest of the analysis, as it was found to be insensitive to this effect in studies with cosmic muons [11].
- The resulting mean energies obtained for the different ions were then divided by those extracted from the GEANT4 simulations in a similar fashion (Fig. 7) to yield the quenching factors.

The measured quenching factors are displayed as a function of the ion atomic number in Fig. 8. For light, high-energy ions, the quenching factors are found to be greater than 1, i.e. the measured energies are greater than

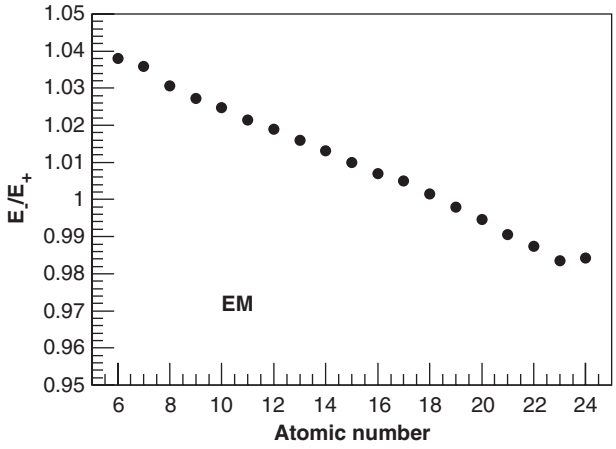

Fig. 6. Ratio of the mean energies measured at the two ends of a crystal in the first (horizontal) layer, as a function of the ion atomic number.

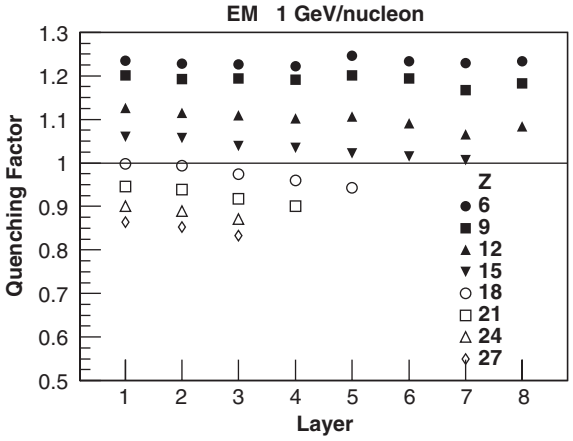

Fig. 9. Ratio of mean measured/calculated deposited energies as a function of the EM layer for different ion atomic numbers. The beam energy is 1 GeV/nucleon.

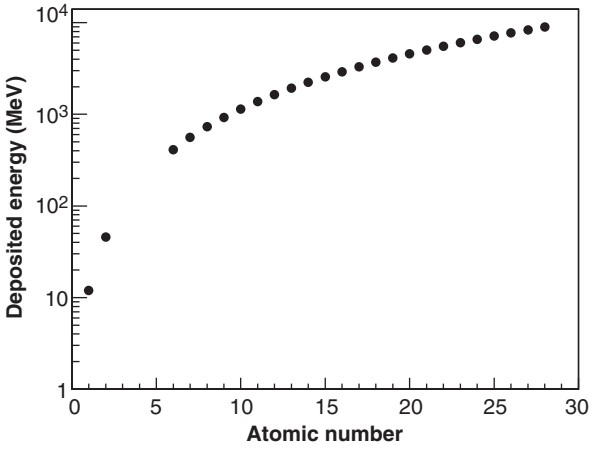

Fig. 7. Average deposited energy for the ionization peak as a function of the ion atomic number, as calculated with GEANT4.

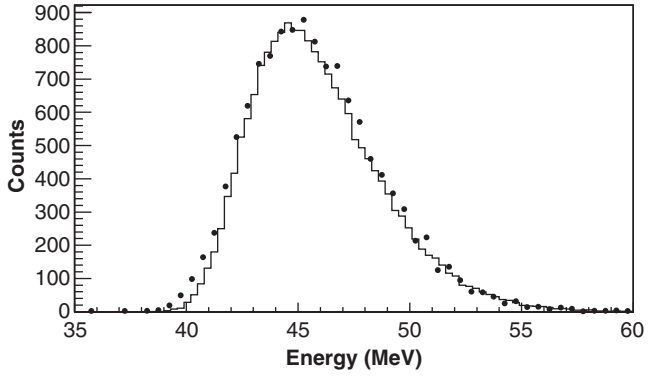

Fig. 10. Comparison between the deposited energy distribution predicted by GEANT4 (histogram) and the measured one (symbols, energy reduced by 5.5%) for 1.7 GeV/nucleon α particles.

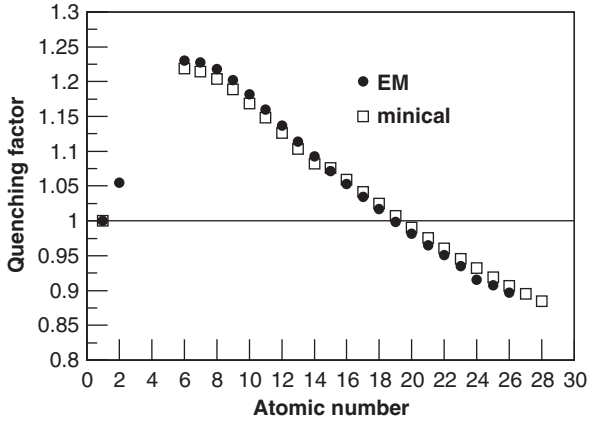

Fig. 8. Measured quenching factors as a function of the particle atomic number. The solid dots (open squares) correspond the EM (Minical) data. The statistical errors are negligible, the systematic uncertainties are estimated to be 3%. The beam energy is 1.7 GeV/nucleon.

the calculated ones by 23% for $Z = 6$ (C). This situation is opposite to that commonly observed at low incident energy where the quenching factors lie below unity. We will refer to this unexpected effect as "antiquenching" in the following. This effect can be tracked down to lower incident energy thanks to the 1 GeV/nucleon data, as some ions approach or reach full stopping in the calorimeter (Fig. 9). For example, a gradual transition toward the known low-energy behavior (quenching factor <1) is observed for $Z = 15$ ions as the ions slow down.

For α-particles, as the distribution is not Gaussian-shaped, the quenching factor has been determined by scaling the calculated deposited distribution so as to best reproduce the measured one. Fig. 10 displays a comparison between measured and calculated deposited energy distributions, the former being scaled by a factor $(1.055)^{-1}$ (no smearing has been applied to the GEANT4 distribution). The quenching factor at 1.7 GeV/nucleon is thus 1.055 ± 0.005.

4. Discussion

4.1. Comparison with other data

As the antiquenching effect was unexpected, multiple cross-checks have been performed. The good agreement between Minical and EM results (Fig. 8) rules out an electronics-related problem, since the Minical makes use of peak-sensing ADCs while the EM ASICs sample the analog signals at a fixed delay time through a Track & Hold stage. It must be emphasized that the longitudinal shower profiles measured at CERN for high-energy electrons ($E > 10$ GeV) and calibrated with the above procedure (using high-energy muons instead of protons) were found [13] to be in very good agreement with the GEANT4 predictions. This agreement demonstrates the validity of the calibration procedure and justifies the implicit assumption that there is no quenching for high-energy electrons, muons and protons. It may be useful to reiterate that the calibration performed with gamma-rays from a ^{22}Na source for the Minical is in excellent agreement with that obtained from protons.

One can wonder if the unexpected high quenching factors observed for light ions are not an artifact arising from the difference in shape of the ionization peaks for ions and protons, which are Gaussian and Landau-like, respectively (in passing, it must be noted that the difference between the mode and average values of the asymmetric distribution calculated for protons is only 6%). This possibility has thoroughly been investigated. Using different assumptions, the maximum deviation of the calibration constants established from the proton distributions is found to be lower than 3%. It is thus excluded that the difference in shape of the distributions is a factor in the observed features.

The deposited energies calculated by GEANT4 were compared to the results of other calculations SRIM [14], NIST [15], GEANT3 [16], different versions of GEANT4, or by simply integrating the Bethe–Bloch formula. The results showed little dispersion, the reference results given by SRIM being 1% and 4% higher than the GEANT4 predictions for C ions and protons, respectively. Using SRIM instead of GEANT4 would actually even increase the ion quenching factors displayed in Fig. 8.

Can the antiquenching effect be due to a physical process at play in the scintillator? As mentioned earlier, quenching is understood as resulting from the excitation of non-radiative degrees of freedom in the scintillator because of the high ionization density arising from the passage of a large-Z ion, bringing about a non-linear light function $L(\Delta E)$, where ΔE is the energy deposited within the crystal. At low incident energy, the effect only depends on $\mathrm{d}E/\mathrm{d}x$ (Birks' Law [12]) but at high energy, it also becomes dependent on the ion Z: at a fixed $\mathrm{d}E/\mathrm{d}x$, the higher Z, the higher β and thus the greater the δ-electron emission, reducing the quenching [7].[1] Since $\mathrm{d}E/\mathrm{d}x$ decreases and the fraction of the energy carried by δ electron increases as the particle energy increases, both factors concur to a reduction in quenching at higher energy.

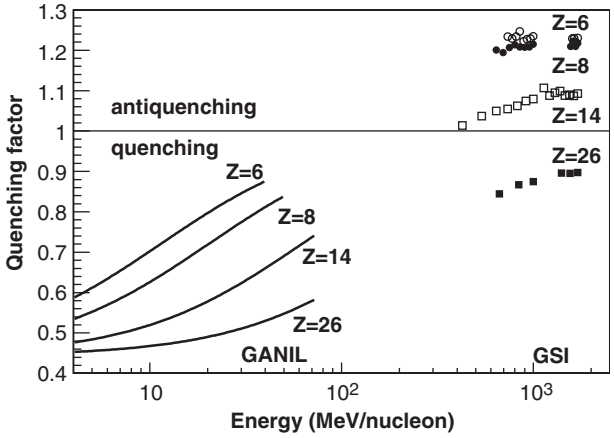

Fig. 11. Compilation of the quenching factors measured at GANIL and GSI as a function of the ion's energy per nucleon, for the different ions relevant to the on-orbit calibration of GLAST's calorimeter.

It is instructive to compare the quenching factors measured at GSI with those obtained [17] in a previous experiment at GANIL below 73 MeV/nucleon (Fig. 11). The latter experiment was performed with the same crystals, PIN diodes and the Minical electronics as at GSI and the data were analyzed with a similar procedure. However, since the ions stopped inside a crystal, the quantity $L(E_{\mathrm{tot}})$ was actually measured (where E_{tot} is the ion incoming kinetic energy), and the quenching factor $\mathrm{d}L/\mathrm{d}E$ was derived by differentiation of the functional fitted on the data. At low incident energy, the expected quenching situation (quenching factor <1) indeed prevails but the quenching factors rise with the ion energy, as expected from the above considerations. The GSI data fall rather nicely in the trend of the GANIL data.

From Fig. 11, antiquenching is thus not as surprising as it may first appear. However, why a light ion leads to more light per MeV of deposited energy than a proton is unclear. A nuclear effect has been considered, but the observed narrowness of the ionization peaks makes this very unlikely.

4.2. Pulse shape

The "antiquenching" effect indicates a difference in the scintillation process for protons and heavy ions. It thus appears interesting to investigate the time dependence of the light output, which is observed [4] to be different between protons and heavier nuclei at low incident energy (E/nucleon <100 MeV). The light output can be described as the sum of two exponential functions associated with a fast and a slow component:

$$L(t) = L_{\mathrm{tot}}\left[\frac{f}{\tau_{\mathrm{f}}}\exp\left(-\frac{t}{\tau_{\mathrm{f}}}\right) + \frac{(1-f)}{\tau_{\mathrm{s}}}\exp\left(-\frac{t}{\tau_{\mathrm{s}}}\right)\right]$$

[1] Due to their long ranges, δ electrons escape the primary ionization column and leave their energy in a less-dense ionization region.

f being the relative weight of the fast component. Fast and slow components arise from the deexcitation of different states of the scintillator [4]. The fast component corresponds to the radiative capture by Tl activator sites of loosely bound electron–hole pairs (excitons), whose formation is favored at high ionization density. On the other hand, the slow component arises from the capture of individual electrons and holes resulting in the excitation of metastable states not accessible to excitons. This property justifies the use of alkali halides like CsI for pulse-shape identification, a technique widely used in low-energy heavy-ion nuclear physics.

Experimentally, it was found [18] below 30 MeV/nucleon that $\tau_s \simeq 7\,\mu s$ and remains essentially constant for all particles, whereas $\tau_f \simeq 0.5-1\,\mu s$ and varies significantly with the particle nature. The slow component represents more than 30% of the total light yield for protons, while it is almost negligible for heavy ions. In Ref. [7], the pulse shape measured with a phototube for low-energy heavy ions (E/nucleon < 50 MeV) was found to exhibit only one component, having a decay time of 650 ns.

In the relativistic domain, the pulse shapes have not been measured for heavy ions to the best of our knowledge. As a slow component with a decay time longer than several μs is essentially filtered out by the shaping amplifiers, a different feeding of the fast/slow components for $Z = 1$ particles and heavy ions would affect the measured quenching factors and possibly lead to the observed "antiquenching" effect.

This consideration motivated a complementary experiment, which was performed again at GSI with a 1.7 GeV/nucleon C beam. The aim was to measure the shape of the pulses for C ions and compare it to that obtained for $Z = 1$ particles. Pulses from CsI crystals read out either with a fast Photonis XP2020 phototube or from a photodiode associated with a charge preamplifier were recorded with a digital oscilloscope, serving as a flash-ADC. The digitization results were transferred in real time via a GPIB interface to a PC.

The pulses with corresponding fits are displayed in Figs. 12 and 13 for cosmic muons (left) and C ions (right). For the phototube, a rise time of 50 ns has been considered in the fit, while the transfer function of the charge-sensitive preamplifier has been assumed to be that of a perfect integrator with a decay time of 93 μs. The fit values on the figures correspond to the time constant of the fast component (τ_f), to the time constant of the slow component (τ_s) and the fraction of the total represented

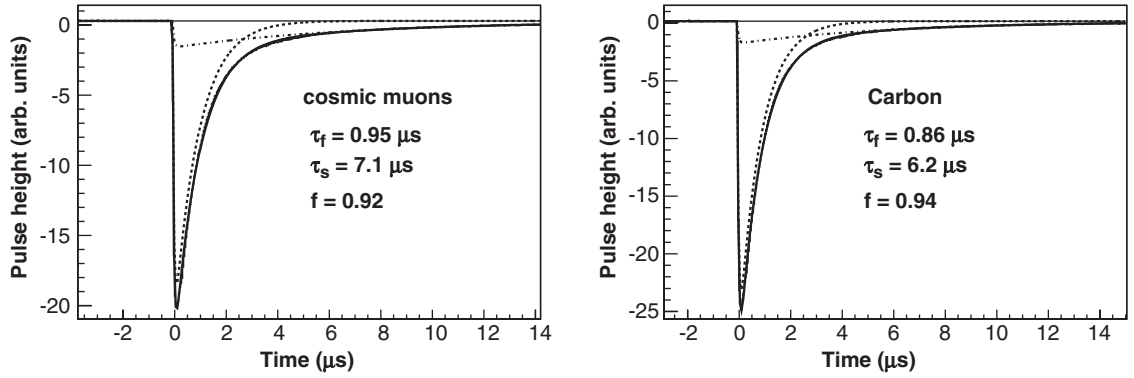

Fig. 12. Left: pulse (averaged over 325 events) measured with the phototube for cosmic muons. The superimposed curves correspond to fits: fast component (dashed), slow component (dot–dashed), total (solid). Right: same (pulse averaged over 58 events) for 1.7 GeV/nucleon C ions.

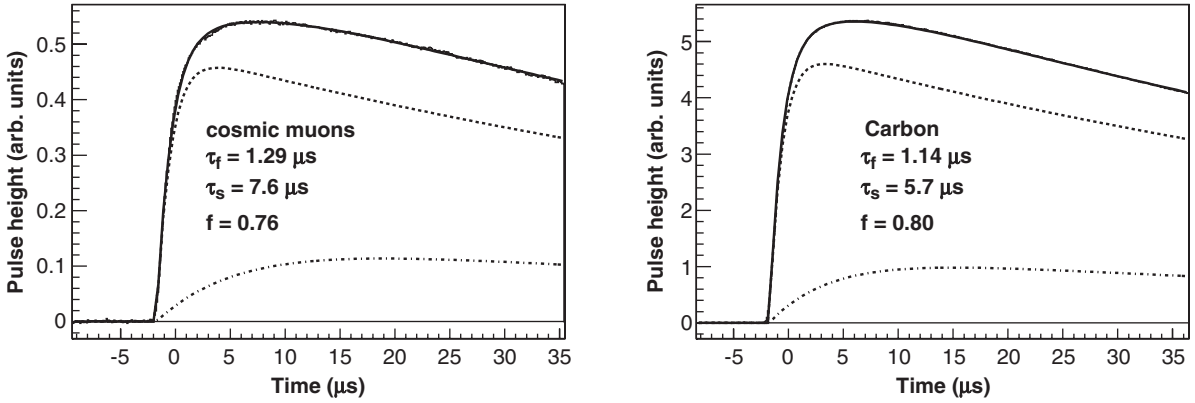

Fig. 13. Left: pulse (averaged over 15 events) measured with the photodiode + charge preamplifier for cosmic muons. The superimposed curves correspond to fits: fast component (dashed), slow component (dot–dashed), total (solid). Right: same (pulse averaged over 23 events) for 1.7 GeV/nucleon C ions.

by the fast component (f). Please note that the relative weight of the slow component is found to be different for the two detectors, an effect probably due to the different wavelength sensitivity for the photodiode and the photo-tube. The most important feature, however, is that for both detectors, the pulse shapes are observed to be nearly identical for muons and C ions, with a significant slow component in both cases. This similarity in the pulse shape is at odds with what would be expected from a naive extrapolation of the behavior prevailing at lower energy, and makes the interpretation of the antiquenching effect a little more challenging.

5. Energy resolution

The GSI data also provide a very convenient way to investigate the energy resolution of the crystals since the deposited energy through ionization varies between about 500 MeV for C ions to over 8 GeV for Fe ions (Fig. 7) and the distributions are narrow. For protons, as mentioned above, the GEANT4 distributions, well fit by Landau functions, had to be smeared by 0.6 MeV to match the observed ones well, i.e. about 5% of the mean energy. The same effect was seen with cosmic muons. It must be stressed that the energy distributions observed at the two ends of the crystals are well correlated, proving that this 5% dispersion is intrinsic in the light production and not due to the light collection process or underestimated electronic noise.

In contrast to the proton case, the distributions for heavy ions assume a Gaussian shape. The widths (RMS) of the distributions measured for the first Minical layer are displayed in the top panel of Fig. 14 as a function of the ion atomic number (open squares). For comparison, also shown in the panel are the GEANT4 corresponding values (solid dots). The experimental widths exceed the expected ones by a fairly constant factor of 30%. The relative widths, obtained by dividing the widths by the corresponding mean energies are plotted in the bottom panel of Fig. 14. The same exercise was repeated for the first layer of the EM. For the data associated with atomic numbers between 8 and 20 (HEX8 range), the electronic noise is not negligible, the contribution deduced from the pedestal width amounting to about 6 MeV (for the energy summed over the two ends as considered here). Once this effect is taken in account, there is a fair agreement between the EM and Minical values.

Two different prescriptions regarding the resolution dependence on the deposited have been tested, corresponding to the two curves displayed in the bottom panel of Fig. 14. The thick curve corresponds to a constant instrumental resolution of 0.55% added quadratically to the calculated relative widths. A good agreement with the data is obtained for all ions, but the 5% dispersion observed for protons is inconsistent with this prescription. The thin curve corresponds to a prescription assuming a stochastic term (scaling as $1/\sqrt{E}$) added quadratically to the constant

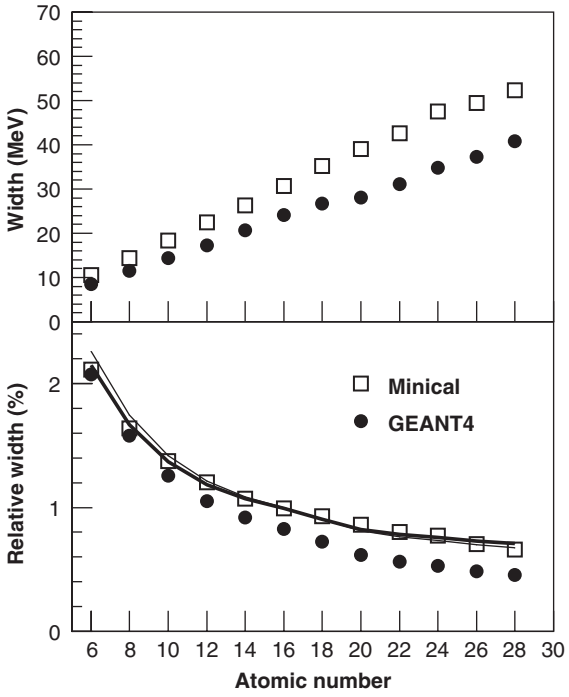

Fig. 14. Top: widths of the measured (open squares) and calculated (solid dots) ionization peaks plotted as a function of the ion atomic number. Bottom: same as top for the relative widths. The curves correspond to the two prescriptions described in the text.

term ($\sigma_E/E = \sqrt{a_0 + a_1/E}$), a_0 and a_1 being adjusted so as to reproduce simultaneously the resolutions found for protons and Ni ($Z = 28$). The adjusted values are $a_0 = 0.212$ and $a_1 = 297$ MeV. The thin curve slightly overshoots the data for ions with Z lower than 10. Besides this slight discrepancy, such a non-negligible stochastic term (only required to account for the proton data) is hard to reconcile with the large number of photo-electrons collected (about 800/MeV for the small diode).

The instrumental energy resolution deduced from these data is negligible with respect to the dispersion in the deposited energy prevailing for the electromagnetic showers to be measured in orbit. In consequence, it will not contribute significantly to the reconstructed-energy resolution.

6. Loss to nuclear reactions

In orbit, a large fraction of the ions traversing the calorimeter will undergo nuclear reactions. This fraction can be extracted from our data, as nuclear reactions lead to a gradual depletion of the ionization peaks for deeper layers. Fig. 15 displays the peak yield as a function of the layer number for different ion atomic numbers. The charge-changing cross-section, σ can be estimated from an exponential fit on the points of Fig. 15, since the yield for layer i, y_i can be written as a function of the average depth d_i as $y_i = e^{-d_i\sigma}$. The resulting cross-sections are compared to the total reaction cross-sections of Tripathi

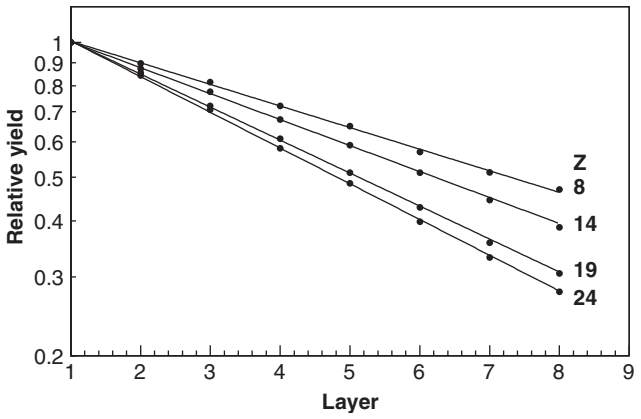

Fig. 15. Experimental yield of the ionization peak normalized to that of the first layer as a function of the layer number, for ions with $Z = 8$, 14, 19 and 24 (semi-logarithmic scale). The data were measured with the Minical. The lines correspond to exponential fits to the data.

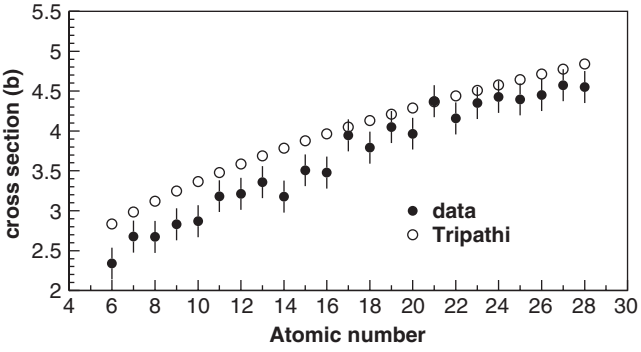

Fig. 16. Experimental cross-sections deduced from the decrease in yield of the ionization peak as a function of the ion atomic number (solid dots). The Tripathi cross-sections are shown for comparison (open dots).

[19] in Fig. 16. A reasonable agreement is found, the measured charge-changing cross-sections being slightly lower than the total reaction cross-sections, as expected.

7. Conclusions

The response of the GLAST CsI calorimeter to heavy ions similar to the cosmic rays in orbit has been studied in an experiment performed at GSI with the FRS. The observed "antiquenching" effect is unexpected but is compatible with the trend established at lower energy. The similarity in the pulse shapes observed for $Z = 1$ particles and C ions enhances the challenge to devise a simple explanation for this feature.

Whatever explanation holds, the quenching factors measured for ions can be used for the in-flight calibration as long as they can be safely extrapolated to higher energies, 90% of the cosmic-ray ions having an energy in the range 1.5−10 GeV/nucleon according to CREME [3]. The quenching-factor dependence on the ion energy is actually found to be negligible between 1.0 and 1.7 GeV/nucleon (Fig. 11), while dE/dx varies by 7% in this range. The quenching-factor uncertainty associated with the measurement and the extrapolation to the energy domain relevant to GLAST is estimated to be better than 3%.

Acknowledgments

It is a pleasure to thank the accelerator team at GSI for providing high-quality beams. We are very grateful to W. Trautmann, K. Boretzky and Th. Aumann for their help in the complementary run performed at GSI. Enlightening discussions with Joel Galin are acknowledged.

References

[1] GLAST Science Brochure: ⟨http://glast.gsfc.nasa.gov/public/resources/pubs/gsd/GSD_print.pdf⟩.
[2] LAT web page: ⟨http://www-glast.stanford.edu⟩.
[3] A.J. Tylka, et al., IEEE Trans. Nucl. Sci. NS-44 (1997) 2150.
[4] W.R. Leo, Experimental Techniques for Nuclear and Particle Physics, second ed., Springer, Berlin, p. 168.
[5] R.B. Murray, A. Meyer, Phys. Rev. 122 (1961) 815.
[6] R.C. Powell, L.A. Harrah, J. Chem. 55 (1971) 1878.
[7] M. Parlog, et al., Nucl. Instr. and Meth. A 482 (2002) 674 and references therein.
[8] M.H. Salamon, S.P. Ahlen, Phys. Rev. B 24 (1981) 5026.
[9] S.M. Schindler, et al., Proceedings of the 18th International Cosmic Ray Conference, vol. 8, Bangalore, 1983, 73pp.
[10] GEANT4: ⟨http://wwwasd.web.cern.ch/wwwasd/geant4/geant4.htm⟩.
[11] J. Ampe, et al., IEEE Trans. Nucl. Sci. NS-51 (5) (2004) 2008.
[12] J.B. Birks, The Theory and Practice of Scintillation Counting, Pergamon, New York, 1964.
[13] B. Lott, et al., in preparation.
[14] SRIM ⟨http://www.srim.org/SRIM/SRIM2003.htm⟩.
[15] NIST ⟨http://physics.nist.gov/PhysRefData/Star/Text/programs.html⟩.
[16] GEANT3: ⟨ http://wwwasd.web.cern.ch/wwwasd/geant/⟩.
[17] J. Bregeon, Ph.D. Thesis, University of Bordeaux, France, 2005.
[18] F. Benrachi, et al., Nucl. Instr. and Meth. A 281 (1989) 137.
[19] R.K. Tripathi, et al., Nucl. Instr. and Meth. B 117 (1996) 347.